Tectonophysics 495 (2010) 315–323

Contents lists available at ScienceDirect

Tectonophysics

journal homepage: www.elsevier.com/locate/tecto

Episodic exhumation of the Greater Himalayan Sequence since the Miocene constrained by fission track thermochronology in Nyalam, central Himalaya

An Wang [a,b,*], John I. Garver [c], Guocan Wang [a,b], Jacqueline A. Smith [d], Kexin Zhang [a,b]

[a] State Key Laboratory of Geological Processes and Mineral Resources, China University of Geosciences, Wuhan 430074, China
[b] Faculty of Earth Sciences, China University of Geosciences, Wuhan 430074, China
[c] Geologic Department, Union College, Schenectady NY 12308, USA
[d] Department of Physical and Biological Sciences, The College of Saint Rose, Albany NY 12203, USA

ARTICLE INFO

Article history:
Received 15 June 2010
Received in revised form 23 September 2010
Accepted 24 September 2010
Available online 1 October 2010

Keywords:
Fission track
Thermochronology
Himalaya
Nyalam
Tibet

ABSTRACT

The Greater Himalayan Sequence (GHS), which makes up the core of the Himalayan orogen, has an uppermost tectonic contact defined by the South Tibetan Detachment System (STDS) and a lower tectonic contact defined by the Main Central Thrust (MCT). The GHS occurs as one of the most important tectostratigraphic units for deciphering processes related to tectonic and climatic exhumation across the orogen. Zircon and apatite fission track (ZFT, AFT) dating were carried out along a transect in Nyalam, central Himalaya in southern Tibet to constrain cooling driven by orogenic process since the middle Miocene. The hanging wall of the STDS yields an essentially unreset Jurassic ZFT age in the Jurassic strata. However, below the STDS within the GHS there is a clear and distinct thermal signal of cooling related to exhumation. In the footwall and within the GHS, the rocks have ZFT ages of middle Miocene to Pliocene, and AFT ages of late Miocene to Quaternary that get younger downward and away from the STDS. In combination with thermal structure modeling, a two-part episodic model, which is widely compatible with existing thermochronological data, is proposed for cooling and exhumation of the GHS since the middle Miocene: [1] middle Miocene; and [2] Pliocene to Quaternary (Recent). The middle Miocene cooling is suggested to have resulted from a rapid tectonic unroofing by down-to-the-north slip on the STDS. The tectonic exhumation was also recorded by several other thermochronological systems (e.g. biotite $^{40}Ar/^{39}Ar$) with concordant middle Miocene cooling ages in different structural positions across the GHS. Post middle Miocene ZFT and AFT cooling ages in the lower part of the GHS suggest accelerated cooling by climate-enhanced erosional exhumation, which was initiated in the late Miocene to Pliocene and was dramatic in the Quaternary to Recent. Thermochronological data and modeling further imply that the present Himalayan topographic front may have been shaped essentially by surface erosion since the late Miocene, when the Himalayan divide might have been some 20–30 km to the south of its present position. However, these data do not preclude the possibility that the intense erosional exhumation may have triggered rock uplift to approach and/or maintain a steady topography in the GHS.

1. Introduction

The Himalayan orogen has formed since the Eocene due to closure of the Tethyan Ocean driven by convergence of the India and Asian plates (Searle et al., 1987; Beck et al., 1995). The first-order structure of this spectacular orogenic belt is characterized by continental collision accompanied by regionally extensive along-strike faults that accommodate both contraction and extension (Burchfiel et al., 1992; Hodges et al., 1992; Wu et al., 1998; Yin, 2006). Traditionally the Himalayan Orogen is divided by orogen-parallel faults into three major tectostratigraphic units: the Tethyan Himalayan Sequence (THS), Greater Himalayan Sequence (GHS) and Lesser Himalayan Sequence (LHS). The GHS constitutes the core of the Himalayan orogen and the top of this sequence is defined by the extensional South Tibetan Detachment System (STDS) while the bottom is defined by the Main Central Thrust (MCT). A widely held view is that there has been simultaneous motion on the STDS and MCT and therefore southward extrusion of the GHS might driven by ductile flow in the lower crust and significant near-surface exhumation (Hodges et al., 1992; Dezes et al., 1999; Beaumont et al., 2001; Harris, 2007).

The timing of movement on these key boundary faults is debated and poorly known. For example, new chronologies in the central and western Himalaya support a Pliocene–Quaternary activation for the MCT (Jain et al., 2000; Catlos et al., 2001, 2002; Holland et al., 2003; Robert et al., 2009), while little evidence has been identified for Pliocene slip on the STDS. As such, a few workers have suggested that the GHS might have been variably extruded both spatially and

* Corresponding author. Faculty of Earth Sciences, China University of Geosciences, Wuhan 430074, China. Tel.: +86 27 67885097; fax: +86 27 67883002.
E-mail address: anwang@hotmail.com (A. Wang).

0040-1951/$ – see front matter
doi:10.1016/j.tecto.2010.09.037

temporally (i.e. Burbank, 2005; Harris, 2007). Intense surface denudation and exhumation of rocks in the greater Himalaya are considered to be dynamically linked with fault movement (Beaumont et al., 2001; Wobus et al., 2003, 2005; Harris, 2007). However, evidence for the link and mechanisms for this dynamic interaction remain poorly resolved. A comprehensive low-temperature thermochronological evolution of GHS bounded between STDS and MCT is thus essential for understanding and examining both boundary fault activation and surface processes that drive exhumation of rock through erosion, which is largely related to uplift and dramatic climate change that has resulted in intense glaciation.

In this paper, we present new zircon and apatite fission track (ZFT and AFT) ages from rocks taken along a north–south trending transect from the THS to GHS in the Nyalam area (28°N, 86°E; Figs. 1 and 2). This transect crosses the root zone of the GHS and is located in the central Himalaya ~90 km to the west of Mt. Everest (Qomolangma). Based on existing thermochronological data and thermal structure modeling, we address tectonic and climatic exhumation processes of the GHS since the middle Miocene.

2. Geological background

The STDS in the study area is locally referred as the Nyalam detachment (Burchfiel et al., 1992; Dougherty et al., 1998; Wang et al., 2006), which juxtaposes unmetamorphosed and low-grade Tibetan strata of THS over high-grade metamorphic rocks of GHS, which are mainly composed of pelitic schists and gneisses of Precambrian age (Burg et al., 1984; Burchfiel et al., 1992; Wang et al., 2006; Yin, 2006). The main detachment fault is indicated by a ~400 m-thick mylonite belt at the top of the GHS that has a strong north–northeast-dipping foliation. A normal sense of movement on the detachment is indicated by S–C fabrics and asymmetric augen structures (Wang et al., 2006). In addition, normal sense fabrics also exist across ~8 km in the upper part of the GHS (Wang et al., 2006), where small-scale structures in deformed leucogranites reveal good kinematic indicators of the sense of shear (Scharer et al., 1986; Hodges et al., 1998; Murphy and Harrison, 1999; Searle, 1999).

U/Pb dating of deformed migmatite–granite in the GHS yields a middle Miocene (16.8 ± 0.6 Ma) crystallization age (Scharer et al.,

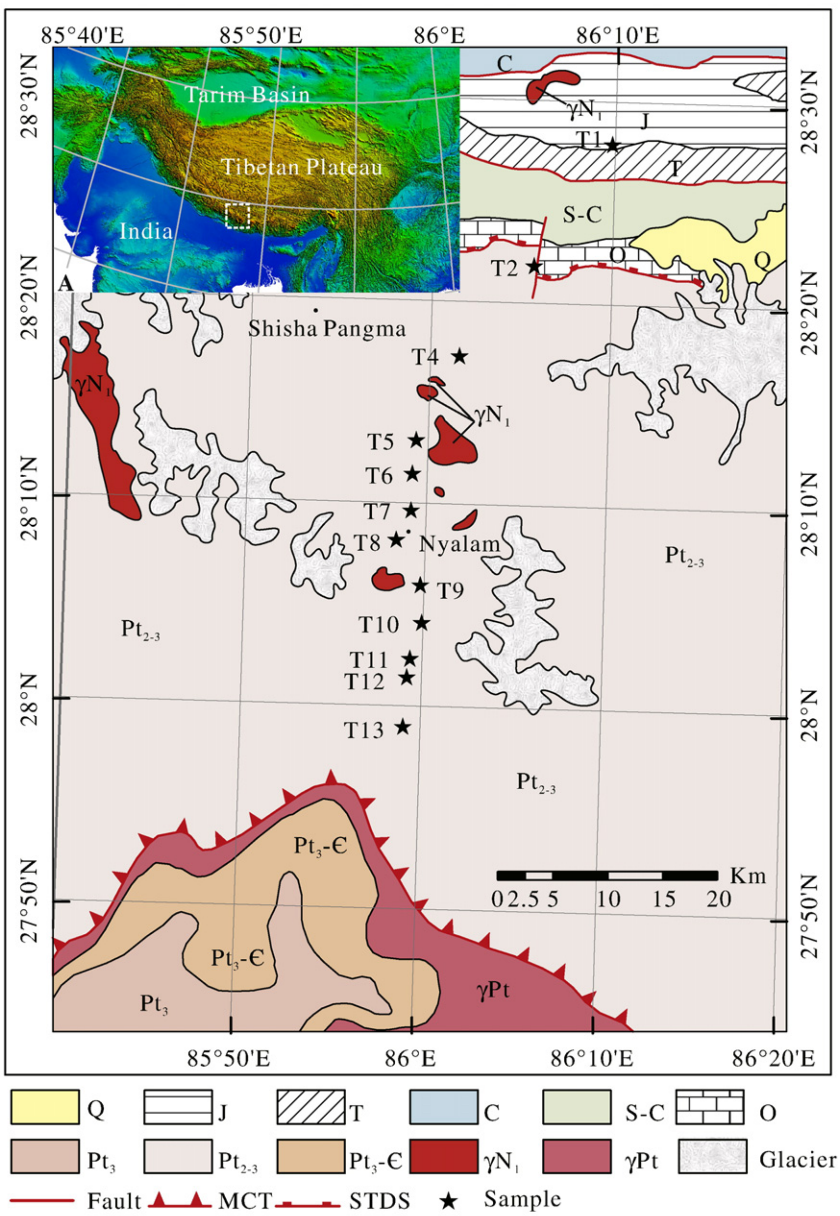

Fig. 1. Simplified geological map of Nyalam area (inset shows location of the studied area in the overall Himalayan orogenic belt). Q is Quaternary; J is Jurassic; T is Triassic; C is Carboniferous; S is Silurian; O is Ordovician; Pt_3 is Neo-Proterozoic; Pt_2 is Meso-Proterozoic; Є is Cambrian; γN_2 is Miocene granite; γPt is Proterozoic granite.

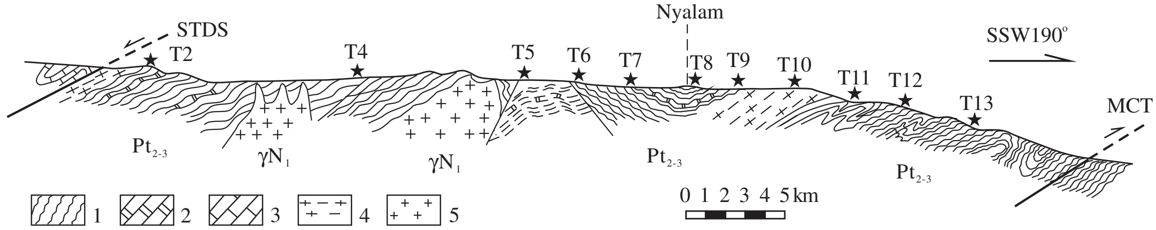

Fig. 2. A simplified geological section across the GHS in the Nyalam transect (modified from 1:250,000 China regional geological survey report). Locations of the STDS and MCT are indicated. Major lithological units are indicated at bottom: 1) gneiss; 2) marble; 3) limestone; 4) mylonite; and 5) granite. Stars indicate fission track sample locations. The section trend is indicated by an arrow at the top right corner. Other abbreviations are listed in the caption of Fig. 1.

1986). Within the Nyalam detachment zone, $^{40}Ar/^{39}Ar$ cooling ages on mica are between 14.8–16.1 Ma at several locations (Wang et al., 2006). Because these $^{40}Ar/^{39}Ar$ ages on mica likely constrain a minimum age for ductile deformation (Lee and Sutter, 1991), it is suggested that the fault activation of the Nyalam detachment occurred between 16.8 and 14.8 Ma, which caused syntectonic rock cooling within the GHS (Scharer et al., 1986; Dougherty et al., 1998; Wang et al., 2006). However, the exact temporal and spatial extent of rock cooling due to the STDS extension remains poorly known, especially at low temperatures.

Thrust structures occur to the south of the village of Nyalam, ~25 km to the south of the Nyalam detachment, where the GHS has a pervasive north-dipping foliation with a few conformable granitic mylonites. A major mylonite zone lies to the south of Nyalam, which is well exposed about 2 km along the China–Nepal highway. Fabrics in the mylonite show consistent up-to-the-south thrust motion of ductile deformation and normal sense has not been identified. Brittle faults were identified within the THS and STDS (Burchfiel et al., 1992); however, little has been reported within the GHS in the area. The surface trace of the MCT along this transect is exposed to the south of Tibet, in Nepal. Previous studies indicate that the MCT initiated its activity in the early Miocene (Le Fort, 1975; Hodges et al., 1992; Godin et al., 2001).

3. Methods

3.1. Sampling

Field survey and sampling were carried out along the China–Nepal highway, which crosses the GHS. In total, twelve samples were collected, one of which was from the hanging wall of the Nyalam detachment and other eleven were from the footwall (Fig. 2). The only hanging wall sample (T1; above the STDS) was collected in the Early–Middle Jurassic strata ~10 km north of the surface trace of the Nyalam detachment. The other eleven samples collected within the GHS are of either gneissic or granitic lithology.

3.2. Fission track methods

Fission track samples were prepared for analysis by the external detector method (Gallagher et al., 1998). ZFT sample preparation and counting were processed in fission track laboratory at Union College in the USA (Garver et al., 1999; Bernet and Garver, 2005). Etching of polished zircon samples was carried out in a NaOH and KOH eutectic at a constant temperature of 228 °C in a thermostatically controlled laboratory oven for 25 h. Fission track mounts were irradiated at the Oregon State nuclear reactor with a nominal thermal neutron fluence of ~2×10^{15} cm^{-2} that was monitored and calibrated by CN5 glass monitors. Low-uranium mica was used as external detector, and after irradiation these were etched in 48% HF at room temperature for 18 min. A zeta calibration factor of 344 ± 5 was determined by independently irradiated zircon standards including Fish Cannon Tuff (USA) and Buluk Member Tuff (Kenya). Counting was carried out using an Olympus BMAX-60 microscope under a magnification of 1250 ($100\times10\times1.25$) equipped with an auto-positioning stage.

AFT slide preparation and counting were processed in the State Key Laboratory of Geological Processes and Mineral Resources in the China University of Geosciences (Wuhan). Apatites were etched in 5 N HNO_3 at room temperature for 18 s. Thermal neutron irradiation was carried out at the China Institute of Atomic Energy with a nominal thermal neutron fluence of ~8×10^{15} cm^{-2}. For AFT, a zeta calibration of 97.4 ± 5.1 was calculated using Durango apatites (USA). AFT counting was carried out under a magnification of 1000 (100×10) with a Zeiss microscope (Wuhan, China).

In case of a simple monotonic cooling, a fission track age represents the time since a sample cooled below its effective closure temperature (i.e. see Reiners and Brandon, 2006). In this sort of application, a linear relationship between thermochronological age and elevation is typically used to estimate long-term exhumation rates. However, in active convergent orogens as the Himalaya, high relief topography and non-vertical exhumation pathway may invalidate such (1-D) interpretation and lead to significant errors (Stüwe et al., 1994; Ehlers and Farley, 2003; Reiners, 2007).

4. Results

4.1. Zircon fission track ages

We were successful in determining a number of new ZFT and AFT ages for this area (Table 1). T1 from the THS in the hanging wall of the Nyalam detachment yielded a ZFT central age of ~189 Ma. All other samples collected within the GHS yielded very young reset ZFT ages mainly in the middle Miocene to Pliocene (~16–3.0 Ma), which are compatible with previously reported biotite $^{40}Ar/^{39}Ar$ (Dougherty et al., 1998; Wang et al., 2006) and AFT ages (Wang et al., 1998).

ZFT ages within the GHS show a spatially distinctive pattern that consists of two apparent age clusters: [1] middle Miocene; and [2] Pliocene (Figs. 3 and 4). The middle Miocene cluster consists of four samples (T2–T7) extending ~25 km from the Nyalam detachment (STDS) to the village of Nyalam, with ages mainly between ~13 and 15 Ma. In this cluster, T6 is excluded. This sample has a relatively large error and it is the only sample that failed the χ^2 test because only a limited number grains could be counted and these counted grains appear to have large grain-to-grain heterogeneity (see Table 1). The samples with Pliocene cooling ages (T9–T12) occur within ~10 km of each other and these samples have ZFT ages between ~3 and 5 Ma. It is worth noting that there appears to be little correlation between age and elevation within the middle Miocene cluster. However, within the latter Pliocene cluster, ZFT ages show relationship with elevation ($R=0.82$; see Fig. 3). The transitional spatial zone between the above clusters (around T8) appears to be occupied by a narrow belt (~5 km) with high ZFT age-elevation slope (Figs. 3 and 4).

Table 1
Fission track data and sample information of the Nyalam transect.

Sample	Elevation	Grain	ρ_s	N_s	ρ_i	N_i	ρ_d	N_d	n	$P(\chi^2)$	Age	-1σ	$+1\sigma$	$U\pm2\sigma$	Lithology
T1	4551	Zircon	7.91×10^6	1335	1.81×10^6	305	2.624×10^5	2665	15	0	188.7	–24.1	+27.6	83.8 ± 9.9	Sandstone
T2	4365	Zircon	3.54×10^6	996	1.19×10^7	3357	2.645×10^5	2652	15	1.1	13.4	–0.5	+0.6	551.2 ± 24.5	Granite
T4	4122	Apatite	2.49×10^5	201	5.05×10^6	4079	3.424×10^6	6847	15	28.6	8.2	–0.7	+0.8	58.8 ± 2.3	Granite
T5	3975	Zircon	3.56×10^6	1529	1.10×10^7	4712	2.666×10^5	2639	15	86.6	14.9	–0.5	+0.5	500.6 ± 20.2	Granitic gneiss
T6	3848	Zircon	9.22×10^6	948	1.97×10^7	2029	2.688×10^5	2626	7	0	16.1	–0.9	+1.0	897.4 ± 47.2	Granitic gneiss
		Apatite	5.03×10^4	29	2.19×10^6	1263	3.405×10^6	6809	15	98.9	3.8	–0.7	+0.8	23.9 ± 1.8	
T7	3753	Zircon	3.08×10^6	1085	1.14×10^7	4016	2.709×10^5	2613	15	10.9	12.6	–0.5	+0.5	512.7 ± 21.8	Granite
T8	3770	Zircon	2.45×10^6	783	1.54×10^7	4931	2.720×10^5	2606	15	9.8	7.4	–0.3	+0.3	690.3 ± 27.8	Biotitic plagiogneiss
		Apatite	6.40×10^4	77	4.06×10^6	4884	3.215×10^6	6430	15	87.9	2.5	–0.3	+0.3	50.2 ± 1.8	
T9	3447	Zircon	1.22×10^6	307	1.23×10^7	3097	2.741×10^5	2593	15	72.5	4.7	–0.3	+0.3	547.7 ± 25.2	Granitic mylonite
		Apatite	2.09×10^4	20	1.91×10^6	1832	3.007×10^6	6013	15	93.9	1.6	–0.4	+0.4	25.3 ± 1.3	
T10	3140	Zircon	6.57×10^5	286	7.96×10^6	3466	2.762×10^5	2580	15	72.3	3.9	–0.2	+0.3	350.6 ± 15.7	Granitic mylonite
T11	2917	Zircon	5.09×10^5	50	8.30×10^6	815	2.794×10^5	2561	15	1.3	3.0	–0.4	+0.5	363.0 ± 27.5	Biotitic plagiogneiss
T12	2660	Zircon	7.55×10^5	293	1.06×10^7	4101	2.805×10^5	2554	15	6.7	3.5	–0.2	+0.2	458.4 ± 19.7	Biotitic plagiogneiss
		Apatite	3.05×10^4	31	2.76×10^6	2812	2.703×10^6	5407	15	76.9	1.5	–0.3	+0.3	40.7 ± 1.7	
T13	2450	Apatite	8.89×10^3	6	1.27×10^6	855	2.438×10^6	4876	15	65.3	0.9	–0.4	+0.5	20.7 ± 1.5	Biotitic plagiogneiss

Note: Sample elevation (m) was measured by a handset GPS with barometer. ρ_s is the spontaneous track density (cm^2); N_s is the number of spontaneous tracks; ρ_i is the induced track density (cm^2); N_i is the number of induced tracks; ρ_d is the track density on fluence monitor (cm^2); N_d is the tracks counted on fluence monitor; n is the number of counted grains; $P(\chi^2)$ is the Chi-squared probability (%); Ages (Ma) are determined using the Zeta method and calculated using the computer program and equations in Brandon (1992). Central ages are given if $\chi^2(\%)<1\%$ for zircon and <5% for apatite, otherwise pooled ages are calculated. $U\pm2\sigma$ is the average uranium concentration (ppm). See context for other lab parameters.

4.2. Apatite fission track ages

AFT ages generally fall between ~1 and 8 Ma, which is consistent with the ZFT result presented above, and also with previously published AFT ages from this area (Wang et al., 1998). For a better understanding of the relationship between the ZFT and the AFT result, all fission track data are plotted in Fig. 4. To the east of the studied area and at the top of the GHS near the detachment surface, AFT yields ages of 11.7 ± 1.3 Ma and 9.7 ± 0.7 Ma (Wang et al., 1998). Within the GHS, previous work has shown that AFT ages are between ~8 and <1 Ma at elevations between 4200 and 3260 m (Wang et al., 1998). Unlike the ZFT data, the AFT ages inside the GHS show a simple southward decrease in age.

5. Numerical modeling of thermal structure

5.1. Model parameters

Our fission track ages span the entire GHS that was extruded by two large-scale faults, optimally they need to be interpreted with an understanding of a 3-D structure of the exhumed crust (Stüwe et al., 1994; Garver and Kamp, 2002; Braun, 2005; Blythe et al., 2007). To illustrate how slip on the MCT and STDS may have affected the thermal structure of the GHS, and thus cooling ages, we constructed a 2-D model (Fig. 5) to model the thermal structure of the shallow crust in the middle Miocene (~16–12 Ma), when we infer the STDS was active.

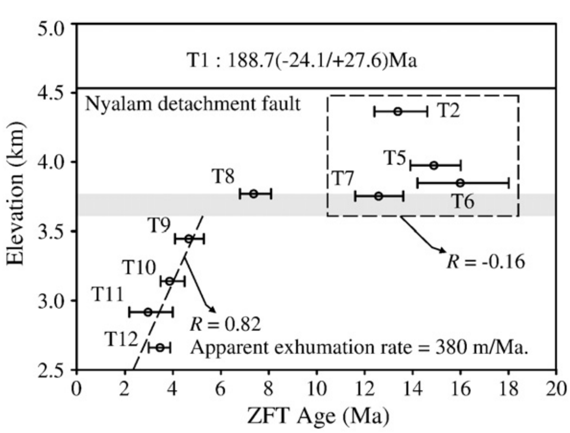

Fig. 3. Age-elevation plot showing ZFT age pattern of the GHS in the Nyalam area. Rocks near T8 marked by shaded swath indicate an approximate divide between the middle Miocene and Pliocene age clusters. A best fit 1-D apparent exhumation rate is indicated for samples T9–T12. Correlation coefficients (*R*) between age and elevation are indicated. ZFT age of T1 in plot is indicated but not plotted.

In this modeling, we assumed a thermal steady and topographic steady state, which are commonly employed (Beaumont et al., 2001; Whipp et al., 2007). A thermal steady state can easily be approached within several million years under high exhumation rates (Stüwe et al., 1994; Whipp et al., 2007). With the intense extension of the STDS, we infer that a thermal steady state was likely achieved during the middle Miocene. We also assume contemporaneous motion on the MCT and STDS (Robinson and Pearson, 2006; Harris, 2007). Previous studies (Dougherty et al., 1998; Wang et al., 2006; Kali et al., 2010; Leloup et al., 2010) indicate that major slip on STDS occurred in the middle Miocene at relatively fast rates. Therefore, we assumed a slip rate of 10 mm/a in our modeling. Possible shear heating generated by movement on the MCT and STDS is local and therefore is not introduced in our modeling. The model domain is ~30 × 100 km^2, which is significantly larger than a spatial distribution of our samples. Other model parameters selected in this study (Table 2) are similar as Whipp et al. (2007) and Ray et al. (2007), validity of which are evaluated by both experiments and applied studies (Beaumont et al., 2001; Whipp et al., 2007).

This study does not make a comprehensive evaluation of thermal structure sensitivity for each model parameter, which has been essentially depicted by Whipp et al. (2007). Rather we focus more on a relationship between the thermal structure and the cooling age pattern along our sample path. Modeling was conducted under six different topographic states to match obtained chronologies in this paper (Fig. 5).

The thermal structure is calculated based on a 2-D steady state thermal advection–diffusion equation:

$$\frac{\lambda}{\rho C}\left(\frac{\partial^2 T}{\partial x^2}+\frac{\partial^2 T}{\partial y^2}\right)-v\left(\frac{\partial T}{\partial x}+\frac{\partial T}{\partial y}\right)+\frac{q}{\rho C}=0, \tag{1}$$

where λ, ρ, C, and q are thermal conductivity, rock density, specific heat and radioactive heat production respectively; v is rock velocity by exhumation and/or fault slipping, and T is temperature. Analysis is conducted using finite element method on a platform of ANSYS.

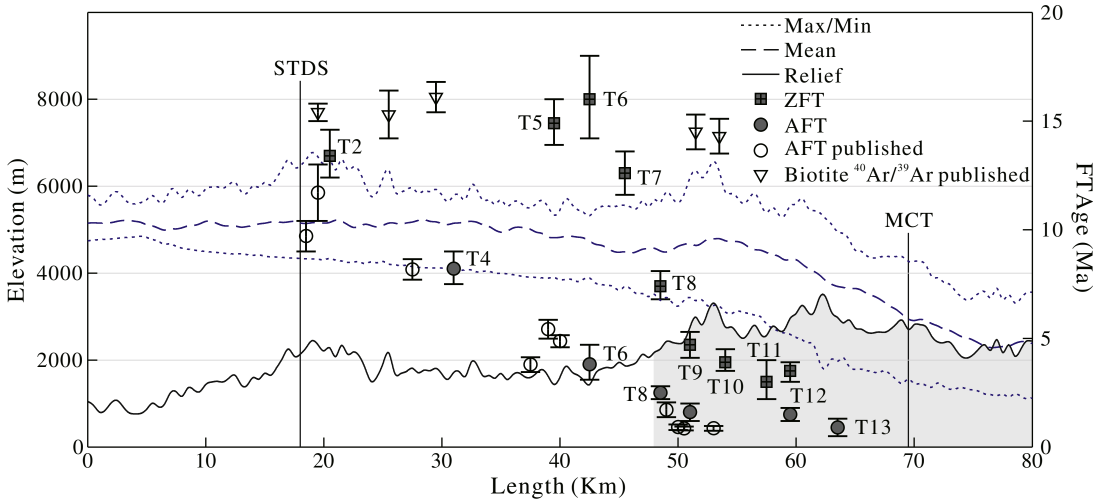

Fig. 4. Spatial distribution of the thermochronological data on a swath topographic profile along the Nyalam transect (N20°E). Chronological data are plotted to the right axis; topographic data are plotted to the left. Hollow circles and triangles indicate published data from Wang et al. (1998, 2006), while filled indicate data obtained in this study. Shaded area indicates an approximate position of the high relief segment referred in Section 6.2. Topographic data were extracted from SRTM3 data (Fielding et al., 1994) by a 30 km wide and 80 km long swath covering the Nyalam transect.

5.2. Thermal structure across the GHS

Before addressing the modeling results, we first make some necessary evaluation of how model parameters affect thermal structure and thus the analysis of fission track ages. Nodal temperatures in modeling are determined by related physical properties and boundary conditions (Table 2), among which basal heat flow is a most influential factor. Higher basal heat flow values produce higher geothermal gradients and thus elevate temperatures at nodal points (Whipp et al., 2007). However, the pattern of the isotherms is relatively insensitive to variation in basal heat flow and/or other physical properties. Major factors affecting the isotherm pattern within the GHS shallow crust include boundary fault slip rates and topographic conditions above the GHS.

Modeling results indicate that simultaneous slip on the MCT and STDS has a combined effect in elevating isotherms within the GHS (Fig. 6). Curvature of isotherms is related to slip rates of the MCT and STDS. However the topographic change (from Nos. 1 to 6) above the GHS tends to elevate isotherms significantly in the southern GHS and it results in a reverse in dip of the overall isotherms (Fig. 6). This result suggests that the overall pattern of low-temperature isotherms is strongly controlled by topography.

Temperature curves along the sample path (Fig. 7) were extracted to illustrate topographic conditions that are most compatible with the thermochronological results. We captured two series of temperature curves as the GHS is cooling by exhumation, in which T2 and T7 are cooling at the ZFT closure temperature respectively (Fig. 7). A reason for this choice is that these two samples mark a range of GHS rocks with the clustered middle Miocene ZFT ages that might be syntectonic with the STDS (see Fig. 4).

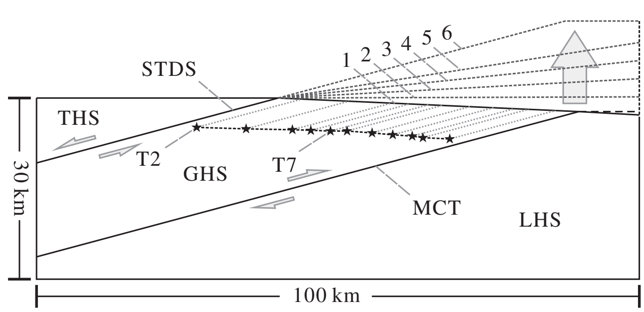

Fig. 5. A 2-D geometric model employed in thermal modeling. Dashed lines marked by numbers 1–6 indicate the six topographic states that are employed as boundary conditions in modeling, in which: (1) indicates the present topography obtained from SRTM3 data; (2–5) indicate possible paleotopographic states, each of which with a ~3 km topographic increment at the right model boundary; (6) indicates a possibly maximum topographic state solely by the STDS extension. Sample locations are indicated by stars marked in the sample path; Exhumation trajectory is indicated by parallel dotted lines.

A key result from this modeling is that the present topography cannot produce a thermal structure that fits observed thermochronological data. Under the present topography, thermal modeling (curves A1 and B1) requires rocks to cool first near the MCT, and finally at the upper of the GHS. Therefore, maximum ages would be predicted near the MCT, while minimum to occur at near the STDS. However, this is clearly not the case as we see the ZFT ages across the GHS with minimum ages near the MCT.

Similarly, we propose that specific paleotopographic conditions compatible with existing thermochronological data along this transect are required to meet three conditions: (1) Rocks along the sample path are required to cool progressively southward from the STDS to MCT because the ZFT ages decrease to the south; (2) When T2 (13.4 ± 0.6 Ma) at the top of the GHS cools below the ZFT closure temperature, the GHS rocks south of T7 must remain below the biotite $^{40}Ar/^{39}Ar$ closure temperature; (3) No rock along the sample path can cool below the AFT closure temperature when T7 (12.6 ± 0.5 Ma) cools at ZFT closure temperature, because almost all AFT ages are less than 10 Ma. Collectively, these suggest that topographic conditions marked between model runs No. 3 and 4 are best candidates.

Table 2
Parameters used in numerical modeling.

Property	Model parameter
Specific heat	800 J/kg K
Conductivity	2.75 W/m K
Density	2800 kg/m^3
Basal heat flow	35 mW/m^2
THS radioactive heat production	0.5 μW/m^3
GHS radioactive heat production	1.9 μW/m^3
LHS radioactive heat production	0.8 μW/m^3
Surface temperature	5 °C
STDS and MCT dip	15°
STDS and MCT slip rate	10 mm/a
Nodel spacing	500 m
Model domain	~30 km × 100 km

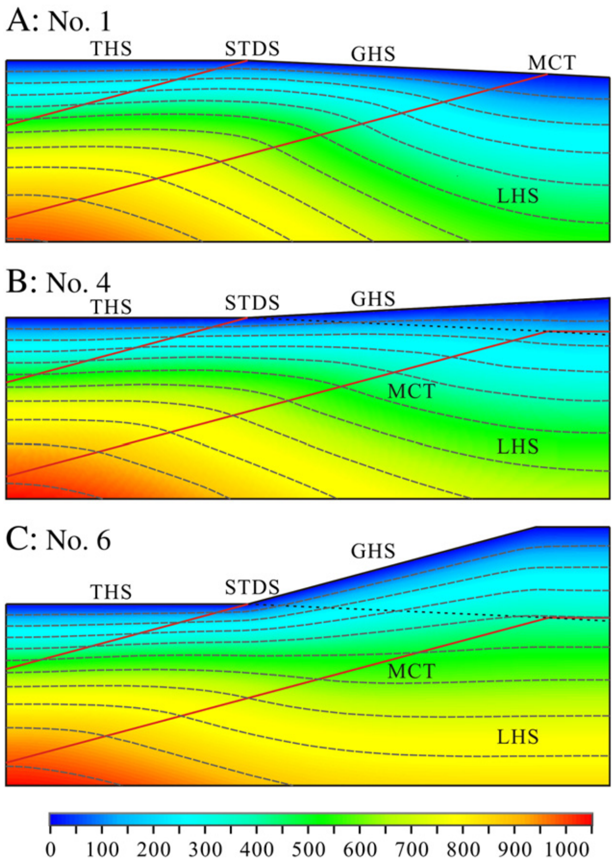

Fig. 6. Modeling results of contour maps showing thermal structure of the GHS under major topographic states: (A) present topography of No. 1, (B) topography of No. 4, and (C) maximum topography of No. 6. Thermal contour interval is 100 ° C. Southward extrusion of the GHS by STDS extension and MCT thrusting tends to raise the isotherms within the shallow parts of the GHS and produces higher geothermal gradients. In addition, the isotherm pattern within the shallow parts of the GHS is strongly affected by different topographic states.

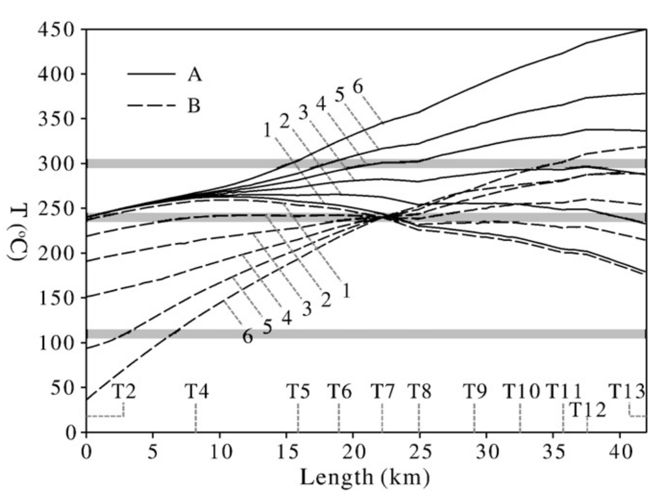

Fig. 7. Temperature curves along the sample path under various topographic states shown in Fig. 5. Lines of series A are temperature curves captured when sample T2 is cooling through the ZFT closure temperature (~240 °C) as the GHS was exhumed, while series B is captured when T7 is cooling at ~240 °C. Shaded swathes indicate approximate biotite $^{40}Ar/^{39}Ar$, zircon and apatite FT partial annealing zones (or effective closure zone). Sample locations are indicated above the length axis. In curves A3 and A4, segments from T2 to T7 are below the biotite $^{40}Ar/^{39}Ar$ annealing zone. In curves B3 and B4, segments near T2 are above the AFT annealing zone. These allow curves 3 and 4 to be the best candidates fit for obtained thermochronological data (see Section 5.2 for a detailed discussion).

6. Discussion

6.1. Tectonic exhumation in middle Miocene

There is little correlation between the fission track ages and sample elevations as is seen in samples T2–T7 that were taken ~25 km across the exposed GHS (Figs. 3 and 4). The ZFT ages are only slightly younger than previously reported muscovite and biotite ages (Dougherty et al., 1998; Wang et al., 2006), as expected because the ZFT system has a lower effective closure temperature. These results imply that samples exhumed through the $^{40}Ar/^{39}Ar$ and ZFT closure temperatures relatively quickly and that ZFT data might provide important insight into the timing of tectonic processes related to this cooling and exhumation compared to the biotite $^{40}Ar/^{39}Ar$ (Wang et al., 2006).

We suggest that slip on the Nyalam detachment probably ceased after ~12 Ma, because there appears to be very limited rock cooling between 12.6 ± 0.5 and 7.4 ± 0.3 Ma (Figs. 3 and 4). In addition, there are no clustered cooling ages that postdate ~12 Ma as indicated by AFT data at the top of the GHS (Fig. 4), which would be predicted if slip on the Nyalam detachment extended after ~12 Ma. These observations suggest that rock cooling was attenuated after ~12 Ma, which may be caused by the end of movement on the STDS in this area. This suggestion is consistent with the timing of the STDS movement history in adjacent areas (Searle et al., 1997; Wang et al., 2006; Kali et al., 2010; Leloup et al., 2010) and central Nepal (Godin et al., 2001). In NW Himalaya, ceasing of STDS motion is also constrained to be by 11–9 Ma (Kumar et al., 1995).

Modeling suggests that both topography and fault slip affected the thermal evolution of the samples in this transect and in our model results, options 3 and 4 are most compatible with measured ZFT and AFT thermochronometers (see Section 5.2). If correct, this result implies that when STDS activation occurred in the middle Miocene, some 6- to 9-km-thick GHS rock exposed by the STDS extension remained over the present southern segment of the GHS. This inference is consistent with the Pliocene ZFT ages and middle Miocene biotite $^{40}Ar/^{39}Ar$ ages (Dougherty et al., 1998; Wang et al., 2006) in the southern segment of the GHS. Furthermore, it is implied that significant topographic development occurred after the middle Miocene.

6.2. Enhanced climatic exhumation since late Miocene

Our data and model result also imply enhanced exhumation since the late Miocene that may be related to an increase in erosional efficiency due to Pliocene and younger climate change. Analysis of 1-D cooling rates of ZFT indicates that cooling likely accelerated since the late Miocene (T8–T9; 7.4 ± 0.3–4.7 ± 0.3 Ma) in the lower part of the GHS (Fig. 3). Quaternary AFT ages in the lower part of the GHS (1.6 ± 0.4–0.9 ± 0.5 Ma) consistently support that exhumational-driven cooling greatly enhanced in the Quaternary (Figs. 3 and 4).

What drove this late Miocene to Quaternary accelerated exhumation? Because the samples with Pliocene ZFT ages lie below a structural thickness to the STDS well beyond the ZFT closure depth, ZFT and AFT ages were not likely related to faulting along the STDS. However, we note that relief in the Nyalam River valley across the lower part of the GHS is 2–3 km (Fig. 4), which is dramatic and in the range of the total closure depth of AFT. In addition, these Pliocene–Quaternary FT ages spatially coincide well with this high relief segment (Fig. 4).

We suggest that accelerated cooling since the late Miocene–Pliocene in the southern GHS was essentially driven by surface erosion facilitated by climate change (largely enhanced precipitation related to the monsoon and glaciation). This inference is supported by the widely accepted view that global cooling and glaciation have intensified since the late Miocene and were prevalent in the Pliocene–Quaternary (An et al., 2001; Huntington et al., 2006). Likewise, elsewhere in the Himalayan front, young ZFT and AFT cooling ages are inferred to have resulted from high erosion driven by climate change (Burbank et al., 2003; Thiede et al., 2004, 2005; Huntington et al., 2006; Whipp et al., 2007).

The acceleration of surface erosion in the Himalayan front is partly supported by remarkable thickness of sediments in the Siwalik foreland basin in the central Himalaya, which indicate that erosion and basin deposition were coupled and have increased since the late Miocene. The lower Siwalik (~12–8 Ma) is characterized by mudstones and fine- to medium-grained sandstone with a thickness of ~1.4 km. The first conglomerate beds appear at ~6 Ma in the middle Siwalik, which is dominated by sandstones. In the upper Siwalik (since ~3 Ma) 1- to 2-m-thick conglomeratic beds are common (Quade et al., 1995; Sanyal et al., 2005).

6.3. Did erosional exhumation triggered rock uplift?

Our modeling and thermochronological data suggest that a ~6- to 9-km-thick cover to the currently exposed GHS rocks was removed from the southern GHS. Removal of this large volume of rock occurred since the late Miocene, when erosional exhumation is inferred to have intensified. If correct, this inference may imply that the Himalayan topographic divide remained at or near the MCT, some 20–30 km south of its present position, and the present high elevation of the Himalaya may have been accomplished by the late Miocene. However, this idea may be complicated if recent erosional–exhumation has been intense enough to trigger rock uplift that resulted in a steady topographic state in the Himalayan front, because, the original thermochronological structure might be modified by differential rock uplift between intensely and weakly exhumed areas. For example, Wobus et al. (2003, 2005) suggest that a large-scale active faulting might be driven by climatic erosion along the physiographic transition zone in the Himalayan front, where further field mapping has identified Quaternary faults that appear to support this suggestion (Hodges et al., 2004). However, further studies are required to examine possible significance of climatically driven tectonics in intensely exhumed Himalayan front (Robert et al., 2009).

6.4. A framework model for exhumation of GHS

Based on the above discussion, we envision a model for exhumation of the GHS in the central Himalaya since the middle Miocene (Fig. 8). We suggest that this model is compatible with not only our data, but also with existing thermochronological data (Maluski et al., 1988; Copeland et al., 1991; Macfarlane, 1993; Vannay and Hodges, 1996; Arita and Ganzawa, 1997; Searle et al., 1997; Dougherty et al., 1998; Wang et al., 1998, 2006; Huntington et al., 2006; Wobus et al., 2006; Blythe et al., 2007; Robert et al., 2009; Leloup et al., 2010).

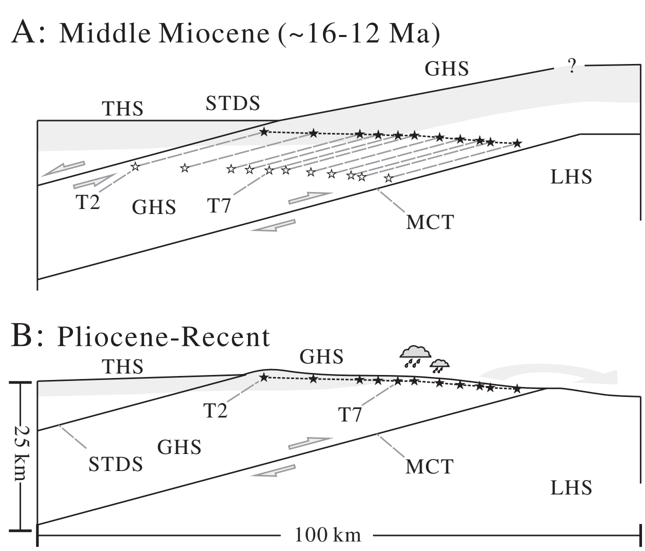

Fig. 8. A model for two-part episodic exhumation of GHS. A: middle Miocene (~16–12 Ma) exhumation by the STDS tectonic unroofing; B: Pliocene to Recent cooling driven by erosional exhumation. Shaded area indicates rocks that were exhumed above the ZFT closure depth during the interval between ~16 and 12 Ma, when the Nyalam detachment was active. Empty stars indicate sample locations at ~16 Ma, while filled stars indicate locations at ~12 Ma. Long dashed lines indicate trajectory of rock exhumation. Arrows indicate fault motion when active. A dip angle of 15° is assumed for STDS and MCT.

This model implies that as the GHS was tectonically exhumed in the middle Miocene, extension of the STDS would be recorded by different thermochronological systems at different structure positions. AFT ages inferred to be syntectonic with the STDS are mainly located at the uppermost part of the GHS (Searle et al., 1997), ZFT ages extend to the central of the GHS, while biotite $^{40}Ar/^{39}Ar$ to near the MCT (Dougherty et al., 1998; Wang et al., 2006). To the west of Nyalam, biotite $^{40}Ar/^{39}Ar$ ages (Copeland et al., 1991—see reinterpretation in Harrison et al. (1997)) abruptly change from middle Miocene to Pliocene southwardly at near the MCT. Similar patterns of cooling ages, which were recorded by the STDS tectonic exhumation affected by subsequent climate-driven erosional exhumation in late Miocene–Pliocene, might also exist in the Larji-Kulu-Rampur-Window in the NW Himalaya (Jain et al., 2000; Vannay et al., 2004; Thiede et al., 2005).

Modeling suggests that erosional exhumation of a ~6- to 9-km-thick crustal section occurred at the southern GHS since tectonic positioning of the GHS by the late Miocene. Most of this erosional exhumation appears to have been accomplished in the Pliocene–Quaternary. This inference is supported by numerous Pliocene–Quaternary fission track cooling ages in the frontal parts of the Himalayan range (Burbank et al., 2003; Hodges et al., 2004; Thiede et al., 2004; Huntington et al., 2006; Blythe et al., 2007). Though the Nyalam detachment (STDS) appears to have become inactive by ~12 Ma, thermochronological data presented in this paper do not preclude possible extrusion of the southern segment of the GHS driven by intense surface erosion. However, the nature and processing of climatically driven rock uplift remain to be constrained by further work (i.e. Hodges et al., 2004; Thiede et al., 2004; Huntington et al., 2006).

7. Conclusions

Thermal modeling combined with our ZFT and AFT dating across a north–south trending GHS root zone in the central Himalaya shows that the thermochronological structure of the present GHS is likely the combined result of two distinct cooling episodes: [1] tectonic exhumation in the middle Miocene (~16–12 Ma), and [2] climate-driven erosional exhumation in the late Miocene–Pliocene (Quaternary).

The middle Miocene episode of tectonic exhumation was facilitated by a slip on the STDS, which caused systematic rock cooling at different structure positions in the GHS, and was recorded by $^{40}Ar/^{39}Ar$, ZFT and AFT thermal domains. Spatial patterns of thermal chronologies suggest that cooling driven by this tectonic exhumation ceased by ~12 Ma, which is considered to be of the end of significant slip on the Nyalam detachment.

The post-middle-Miocene exhumation episode, which appears to have had the strongest effect in the Pliocene–Quaternary and was spatially concentrated in the southern segment of the GHS, is suggested to have been driven by erosion, which was likely facilitated by climate change. If elevated highlands affected global climatic change (Raymo and Ruddiman, 1992; Liu and Yin, 2002), a transfer from tectonic to climatic exhumation in the GHS in the late Miocene may imply that the Himalaya and Tibetan Plateau were brought to present elevations by the late Miocene. This inference is consistent with the preferred paleotopographic conditions by our modeling and with obtained thermochronological data. However, our study does not preclude the possibility that the southern segment of the GHS could be potentially extruded by intense surface erosion in the Pliocene to Quaternary, which is favored by the channel flow model (Godin et al., 2006; Robinson and Pearson, 2006; Harris, 2007).

Acknowledgements

This study was financially supported by the China Geological Survey Institute (1212010610103) and the Natural Science Foundation of China (40902060). ZFT samples were irradiated at the Oregon State Nuclear reactor with financial assistance from the Reactor Use Sharing Program through the US DOE. We express special appreciation to Matt Montario and Eva Enkelmann who provided assistance in sample preparation and fission track dating in Union College. Appreciation also goes to Fabrizio Storti, Marco G. Malusà and an anonymous reviewer, whose suggestions greatly improved an earlier version of this paper.

References

An, Z., Kutzbach, J.E., Prell, W.L., Porter, S.C., 2001. Evolution of Asian monsoons and phased uplift of the Himalayan Tibetan plateau since Late Miocene times. Nature 411, 62–66.

Arita, K., Ganzawa, Y., 1997. Thrust tectonics and uplift process of the Nepal Himalaya revealed from fission-track ages. J. Geogr. 106, 156–167.

Beaumont, C., Jamieson, R.A., Nguyen, M.H., Lee, B., 2001. Himalayan tectonics explained by extrusion of a low-viscosity crustal channel coupled to focused surface denudation. Nature 414, 738–742.

Beck, R.A., Burbank, D.W., Sercombe, W.J., Riley, G.W., Barndt, J.K., Berry, J.R., Afzal, J., Khan, A.M., Jurgen, H., Metje, J., Cheema, A., Shafique, N.A., Lawrence, R.D., Khan, M.A., 1995. Stratigraphic evidence for an early collision between Northwest India and Asia. Nature 373, 55–58.

Bernet, M., Garver, J.I., 2005. Fission-track analysis of detrital zircon. Rev. Mineral. Geochem. 58, 205–237.

Blythe, A.E., Burbank, D.W., Carter, A., Schmidt, K., Putkonen, J., 2007. Plio-Quaternary exhumation history of the central Nepalese Himalaya: 1. Apatite and zircon fission track and apatite [U–Th]/He analyses. Tectonics 26, TC3002. doi:10.1029/2006TC001990.

Brandon, M.T., 1992. Decomposition of fission–track grain–age distributions. Am. J. Sci. 292, 535–564.

Braun, J., 2005. Quantitative constraints on the rate of landform evolution derived from low-temperature thermochronology. Rev. Mineral. Geochem. 58, 351–374.

Burbank, D.W., 2005. Cracking the Himalaya. Nature 434, 963–964.

Burbank, D.W., Blythe, A.E., Putkonen, J., Pratt-Sitaula, B., Gabet, E., Oskin, M., Barros, A., Ojha, T.P., 2003. Decoupling of erosion and precipitation in the Himalayas. Nature 426, 652–655.

Burchfiel, B.C., Chen, Z., Hodges, K.V., Liu, Y., Royden, L.H., Deng, C., Xu, J., 1992. The South Tibetan detachment system, Himalayan Orogen: extension contemporaneous with and parallel to shortening in a collisional mountain belt. Spec. Pap. Geol. Soc. Am. 269, 1–41.

Burg, J.P., Brunel, M., Gapais, D., Chen, G.M., Liu, G.H., 1984. Deformation of leucogranites of the crystalline Main Central Sheet in southern Tibet (China). J. Struct. Geol. 6, 535–542.

Catlos, E.J., Harrison, T.M., Kohn, M.J., Grove, M., Ryerson, F.J., Manning, C.E., Upreti, B.N., 2001. Geochronologic and thermobarometric constraints on the evolution of the Main Central Thrust, central Nepal Himalaya. J. Geophys. Res. 106, 16177–16204.

Catlos, E.J., Harrison, T.M., Manning, C.E., Grove, M., Rai, S.M., Hubbard, M.S., Upreti, B.N., 2002. Records of the evolution of the Himalayan orogen from in situ Th-Pb ion microprobe dating of monazite: Eastern Nepal and western Garhwal. J. Asian Earth Sci. 20, 459–479.

Copeland, P., Harrison, T.M., Hodges, K.V., Maruejol, P., Le Fort, P., Pecher, A., 1991. An early Pliocene thermal disturbance of the Main Central Thrust, central Nepal: implications for Himalayan tectonics. J. Geophys. Res. 96, 8475–8500.

Dezes, P.J., Vannay, J.C., Steck, A., Bussy, F., Cosca, M., 1999. Synorogenic extension: quantitative constraints on the age and displacement of the Zanskar shear zone (Northwest Himalaya). Geol. Soc. Am. Bull. 111, 364–374.

Dougherty, A., Krol, M., Hodges, K., Anonymous, 1998. Miocene tectonic unroofing and cooling of the greater Himalayan sequence, Nyalam region, southern Tibet. Geol. Soc. Am. Abstr. Programs 30, 270.

Ehlers, T.A., Farley, K.A., 2003. Apatite (U–Th)/He thermochronometry: methods and applications to problems in tectonic and surface processes. Earth Planet. Sci. Lett. 206, 1–14.

Fielding, E., Isacks, B., Barazangi, M., Duncan, C.C., 1994. How flat is Tibet? Geology 22, 163–167.

Gallagher, K., Brown, R., Johnson, C., 1998. Fission track analysis and its applications to geological problems. Annu. Rev. Earth Planet. Sci. 26, 519–572.

Garver, J.I., Kamp, P.J., 2002. Integration of zircon color and zircon fission-track zonation patterns in orogenic belts: application to the Southern Alps, New Zealand. Tectonophysics 349, 203–219.

Garver, J.I., Soloviev, A.V., Kamp, P.J.J., Brandon, M.T., 1999. Detrital zircon fission track thermochronology: practical considerations and examples. Mem. Sci. Geol. 51, 454–456.

Godin, L., Parrish, R.R., Brown, R.L., Hodges, K.V., 2001. Crustal thickening leading to exhumation of the Himalayan metamorphic core of central Nepal: insight from U–Pb geochronology and $^{40}Ar/^{39}Ar$ thermochronology. Tectonics 20, 729–747.

Godin, L., Grujic, D., Law, R.D., Searle, M.P., 2006. Channel flow, ductile extrusion and exhumation in continental collision zones: an introduction. Geol. Soc. Spec. Publ. 268, 1–23.

Harris, N., 2007. Channel flow and the Himalayan–Tibetan orogen: a critical review. J. Geol. Soc. Lond. 164, 511–523.

Harrison, T.M., Ryerson, F.J., Le Fort, P., Yin, A., Lovera, O.M., Catlos, E.J., 1997. A Late Miocene–Pliocene origin for the Central Himalayan inverted metamorphism. Earth Planet. Sci. Lett. 146, E1–E7.

Hodges, K.V., Parrish, R.R., Housh, T.B., Lux, D.R., Burchfiel, B.C., Royden, L.H., Chen, Z., 1992. Simultaneous Miocene extension and shortening in the Himalayan Orogen. Science 258, 1466–1470.

Hodges, K.V., Bowring, S.A., Davidek, K.L., Hawkins, D., Krol, M., 1998. Evidence for rapid displacement on Himalayan normal faults and the importance of tectonic denudation in the evolution of mountain ranges. Geology 23, 483–486.

Hodges, K.V., Wobus, C., Ruhl, K., Schildgen, T., Whipple, K., 2004. Quaternary deformation, river steepening, and heavy precipitation at the front of the Higher Himalayan ranges. Earth Planet. Sci. Lett. 220, 379–389.

Holland, B., Marston, R.A., Pandey, A.C., Dubey, C.S., Catlos, E.J., Anonymous, 2003. Geomorphic evidence of recent tectonic activity, MCT Zone, Bhagirathi River valley, Garhwal Himalaya, India. Geol. Soc. Am. Abstr. Programs 35, 171.

Huntington, K.W., Blythe, A.E., Hodges, K.V., 2006. Climate change and Late Pliocene acceleration of erosion in the Himalaya. Earth Planet. Sci. Lett. 252, 107–118.

Jain, A.K., Kumar, D., Singh, S., Kumar, A., Lal, N., 2000. Timing, quantification and tectonic modelling of Pliocene–Quaternary movements in the NW Himalaya: evidence from fission track dating. Earth Planet. Sci. Lett. 179, 437–451.

Kali, E., Leloup, P.H., Arnaud, N., Mahéo, G., Liu, D., Boutonnet, E., Van der Woerd, J., Liu, X., Liu-Zeng, J., Li, H., 2010. Exhumation history of the deepest central Himalayan rocks, Ama Drime range: key pressure–temperature–deformation–time constrains on orogenic models. Tectonics 29, TC2014. doi:10.1029/2009TC002551.

Kumar, A., Lal, N., Jain, A.K., Sorkhabi, R.B., 1995. Late Cenozoic–Quaternary thermo-tectonic history of Higher Himalayan Crystalline (HHC) in Kishtwar–Padar–Zanskar region, NW Himalaya: evidence from fission track ages. J. Geol. Soc. India 45, 375–391.

Le Fort, P., 1975. Himalayas: the collided range—present knowledge of the continental arc. Am. J. Sci. 275, 1–44.

Lee, J., Sutter, J.F., 1991. Incremental $^{40}Ar/^{39}Ar$ thermochronology of mylonitic rocks from the northern Snake Range, Nevada. Tectonics 10, 77–100.

Leloup, P.H., Mahéo, G., Arnaud, N., Kali, E., Boutonnet, E., Liu, D., Liu, X., Li, H., 2010. The South Tibet detachment shear zone in the Dinggye area: time constraints on extrusion models of the Himalayas. Earth Planet. Sci. Lett. 292, 1–16.

Liu, X.D., Yin, Z.Y., 2002. Sensitivity of East Asian monsoon climate to the uplift of the Tibetan Plateau. Palaeogeogr. Palaeoclimatol. Palaeoecol. 183, 223–245.

Macfarlane, A.M., 1993. Chronology of tectonic events in the crystalline core of the Himalaya, Langtang National Park, central Nepal. Tectonics 12, 1004–1025.

Maluski, H., Matte, P., Brunel, M., Xiao, X., 1988. Argon 39–argon 40 dating of metamorphic and plutonic events in the North and High Himalaya belts (southern Tibet, China). Tectonics 7, 299–326.

Murphy, M.A., Harrison, T.M., 1999. Relationship between leucogranites and the Qomolangma Detachment in the Rongbuk Valley, South Tibet. Geology 27, 831–834.

Quade, J., Cater, J.M.L., Ojha, T.P., Adam, J., Harrison, T.M., 1995. Late Miocene environmental change in Nepal and the northern Indian subcontinent: stable isotopic evidence from Paleosols. Geol. Soc. Am. Bull. 107, 1381–1397.

Ray, L., Bhattacharya, A., Roy, S., 2007. Thermal conductivity of higher Himalayan crystallines from Garhwal Himalaya, India. Tectonophysics 434, 71–79.

Raymo, M.E., Ruddiman, W.F., 1992. Tectonic forcing of late Cenozoic climate. Nature 359, 117–122.

Reiners, P.W., 2007. Thermochronologic approaches to paleotopography. Rev. Mineral. Geochem. 66, 243–267.

Reiners, P.W., Brandon, M.T., 2006. Using thermochronology to understand orogenic erosion. Annu. Rev. Earth Planet. Sci. 34, 419–466.

Robert, X., Van Der Beek, P., Braun, J., Perry, C., Dubille, M., Mugnier, J.L., 2009. Assessing Quaternary reactivation of the Main Central thrust zone (central Nepal Himalaya): new thermochronologic data and numerical modeling. Geology 37, 731–734.

Robinson, D.M., Pearson, O.N., 2006. Exhumation of Greater Himalayan rock along the Main Central Thrust in Nepal: implications for channel flow. Geol. Soc. Spec. Publ. 268, 255–267.

Sanyal, P., Bhattacharya, S.K., Prasad, M., 2005. Chemical diagenesis of Siwalik sandstone: isotopic and mineralogical proxies from Surai Khola section, Nepal. Sediment. Geol. 180, 57–74.

Scharer, U., Xu, R.H., Allegre, C.J., 1986. U–(Th)–Pb systematics and ages of Himalayan leucogranites, South Tibet. Earth Planet. Sci. Lett. 77, 35–48.

Searle, M.P., 1999. Extensional and compressional faults in the Everest Lhotse massif, Khumbu Himalaya, Nepal. J. Geol. Soc. 156, 227–240.

Searle, M.P., Windley, B.F., Coward, M.P., Cooper, D.J.W., Rex, A.J., Rex, D., Li, T., Xiao, X., Jan, M.Q., Thakur, V.C., Kumar, S., 1987. The closing of Tethys and the tectonics of the Himalaya. Geol. Soc. Am. Bull. 98, 678–701.

Searle, M.P., Parrish, R.R., Hodges, K.V., Hurford, A., Ayres, M.W., Whitehouse, M.J., 1997. Shisha Pangma leucogranite, South Tibetan Himalaya: field relations, geochemistry, age, origin, and emplacement. J. Geol. 105, 295–317.

Stüwe, K., White, L., Brown, R., 1994. The influence of eroding topography on steady-state isotherms. Application to fission track analysis. Earth Planet. Sci. Lett. 124, 63–74.

Thiede, R.C., Bookhagen, B., Arrowsmith, J.R., Sobel, E.R., Strecker, M.R., 2004. Climatic control on rapid exhumation along the Southern Himalayan Front. Earth Planet. Sci. Lett. 222, 791–806.

Thiede, R.C., Arrowsmith, J.R., Bookhagen, B., McWilliams, M.O., Sobel, E.R., Strecker, M.R., 2005. From tectonically to erosionally controlled development of the Himalayan orogen. Geology 33, 689–692.

Vannay, J.C., Hodges, K.V., 1996. Tectonometamorphic evolution of the Himalayan metamorphic core between the Annapurna and Dhaulagiri, central Nepal. J. Metamorph. Geol. 14, 635–656.
Vannay, J.C., Grasemann, B., Rahn, M., Frank, W., Carter, A., Baudraz, V., Cosca, M., 2004. Miocene to Holocene exhumation of metamorphic crustal wedges in the NW Himalaya: evidence for tectonic extrusion coupled to fluvial erosion. Tectonics 23, TC1014. doi:10.1029/2002TC001429.
Wang, Y., Wang, J., Wang, S., 1998. Fission track evidence for rapid uplift of the Nyalam, Higher Himalaya, Tibet, China. Geol. Rev. 44, 430–434 (in Chinese with English summary).
Wang, Y., Li, Q., Qu, G., Law, R.D., Searle, M.P., Godin, L., 2006. $^{40}Ar/^{39}Ar$ thermochronological constraints on the cooling and exhumation history of the South Tibetan detachment system, Nyalam area, southern Tibet. Geol. Soc. Spec. Publ. 268, 327–354.
Whipp, D.M., Ehlers, T.A., Blythe, A.E., Huntington, K.W., Hodges, K.V., Burbank, D.W., 2007. Plio-Quaternary exhumation history of the central Nepalese Himalaya: 2. Thermokinematic and thermochronometer age prediction model. Tectonics 26, TC3003. doi:10.1029/2006TC001991.
Wobus, C.W., Hodges, K.V., Whipple, K.X., 2003. Has focused denudation sustained active thrusting at the Himalayan topographic front? Geology 31, 861–864.
Wobus, C.W., Heimsath, A., Whipple, K.X., Hodges, K.V., 2005. Active out-of-sequence thrust faulting in the central Nepalese Himalaya. Nature 434, 1008–1011.
Wobus, C.W., Whipple, K.X., Hodges, K.V., 2006. Neotectonics of the central Nepalese Himalaya: constraints from geomorphology, detrital $^{40}Ar/^{39}Ar$ thermochronology, and thermal modeling. Tectonics 25, TC4011. doi:10.1029/2005TC001935.
Wu, C., Nelson, K.D., Wortman, G., Samson, S.D., Yue, Y., Li, J., Kidd, W.S., Edwards, M.A., 1998. Yadong cross structure and South Tibetan detachment in the east central Himalaya (89°–90°E). Tectonics 17, 28–45.
Yin, A., 2006. Cenozoic tectonic evolution of the Himalayan orogen as constrained by along-strike variation of structural geometry, exhumation history, and foreland sedimentation. Earth Sci. Rev. 76, 1–131.